JAAS

Accepted Manuscript

This is an *Accepted Manuscript*, which has been through the Royal Society of Chemistry peer review process and has been accepted for publication.

Accepted Manuscripts are published online shortly after acceptance, before technical editing, formatting and proof reading. Using this free service, authors can make their results available to the community, in citable form, before we publish the edited article. We will replace this *Accepted Manuscript* with the edited and formatted *Advance Article* as soon as it is available.

You can find more information about *Accepted Manuscripts* in the Information for Authors.

Please note that technical editing may introduce minor changes to the text and/or graphics, which may alter content. The journal's standard Terms & Conditions and the Ethical guidelines still apply. In no event shall the Royal Society of Chemistry be held responsible for any errors or omissions in this *Accepted Manuscript* or any consequences arising from the use of any information it contains.

ROYAL SOCIETY OF CHEMISTRY

www.rsc.org/jaas

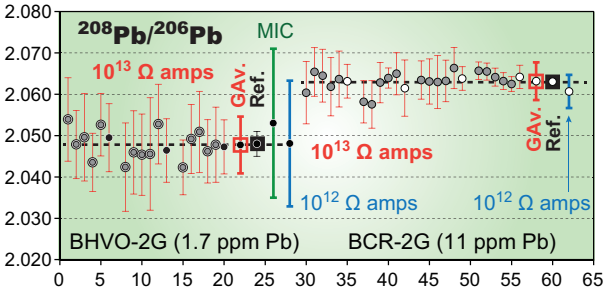

Table of contents entry

Use of 10^{13} Ω amplifiers enabled high precision Pb isotope analysis in situ using UV femtosecond MFC-ICPMS

Draft for JAAS

Technical Note

High-precision *in situ* analysis of Pb isotopes in glasses using 10^{13} Ω resistor high gain amplifiers with ultraviolet femtosecond laser ablation multiple Faraday collector inductively coupled plasma mass spectrometry

Jun-Ichi Kimura,*[a] Qing Chang,[a] Nobuyuki Kanazawa,[b] Satoshi Sasaki,[b] and Bogdan Stefanov Vaglarov[a]

[a*] *Department of Solid Earth Geochemistry, Japan Agency for Marine-Earth Science and Technology (JAMSTEC), 2-15 Natsushima-Cho, Yokosuka 237-0061, Japan*
E-mail: jkimura@jamstec.go.jp; *Fax: +81-46-987-9625; Tel: +81-46-967-9765*

[b] *ThermoFisher Scientific Japan, 3-9 Moriya-Cho, Yokohama 221-0022, Japan*

†Electronic supplementary information (ESI) available. ESI Data Table 1: Representative analytical precisions of Pb isotope ratios obtained by using UVFsLA-MFC-ICPMS with 10^{13} Ω resistor Faraday amplifiers. ESI Data Table 2: Representative analytical results for Pb isotope ratios obtained by using UVFsLA-MFC-ICPMS with 10^{13} Ω Faraday amplifiers. DOI: 10.1039/c4jaxxxxxxx

Abstract

We report high-precision *in situ* determination of Pb isotope ratios in glass samples, using 200 nm ultraviolet femtosecond laser ablation coupled with a multiple Faraday collector–inductively coupled plasma mass spectrometer (MFC-ICPMS), equipped with 10^{13} Ω resistor high gain Faraday amplifiers. The use of the highly sensitive ion interface of MFC-ICPMS together with the state-of-the-art amplifiers enabled determination of $^{208}Pb/^{206}Pb$ and $^{207}Pb/^{206}Pb$ isotope ratios at the highest precision ever achieved from a laser crater with 30 µm diameter and 30 µm depth dug on glass samples containing 1.7–39 ppm Pb. The signal responses of the 10^{13} Ω amplifiers were slower than those of the 10^{11} and 10^{12} Ω amplifiers. We confirmed a strong linear correlation between the rates of signal intensity change for $D^{208}Pbi/dt$ and the measured isotope ratios $[^{20X}Pb/^{206}Pb]/dt$ for the same time intervals. The $D^{208}Pbi/dt$ values deviated around zero, and the $[^{20X}Pb/^{204}Pb]/dt$ value at the zero intercept of the linear regression line represents the Pb isotope ratio of the sample. The slope of the linear regression line was either positive or negative because of different combinations of the amplifiers, indicating that the response of the amplifiers differed individually. The slope also changed with the signal intensity for ^{208}Pbi or $D^{208}Pbi/dt$, *i.e.*, it was flatter at low levels and steeper at high levels. By using these relationships, corrections were made on the time resolved data measured from a single crater. Furthermore, with the proposed analytical method, $^{208}Pb/^{206}Pb$ and $^{207}Pb/^{206}Pb$ isotope ratios in BHVO-2G (1.7 ppm Pb) and BCR-2G (11 ppm Pb) basalt glass samples were analysed by using National Institute of Standards and Technology (NIST) standard reference material (SRM) 612 (38.57 ppm Pb) synthetic glass as an external standard. The laboratory bias of the basalt glass samples was ±0.05–0.15 ‰RD (*per mille* relative difference) and intermediate precisions were ±3–7 ‰ 2 SD (*per mille* 2 standard deviation) for BHVO-2G and ±0.6–3.7 ‰ 2 SD for BCR-2G. These intermediate precisions, along with repeatability, were approximately 2–3 times better than those obtained by either multiple ion counter ICPMS or MFC-ICPMS with 10^{12} Ω resistor amplifiers.

Abstract (349)

1. Introduction

Progress in *in situ* analysis of the Pb isotope ratios, $^{208}Pb/^{206}Pb$ and $^{207}Pb/^{206}Pb$, from small amounts of glass samples has revealed a large heterogeneity of magma sources in both the Earth's mantle and crust.[1-4] This could not have been obtained by bulk rock analysis because the sample preparation[4] requires the homogenization of a considerable amount of sample. However, high-precision analyses can be achieved with this technique, including ^{204}Pb-based isotope ratios.[5, 6]

The advantages of *in situ* Pb isotope analysis were first highlighted by secondary-ionization mass spectrometry (SIMS) applications.[7] This was followed by the application of laser ablation (LA)–multiple Faraday collector (MFC)–inductively coupled plasma mass spectrometry (ICPMS) instrumentation equipped with various ultraviolet nanosecond laser ablation (UVNsLA) systems.[8, 9] The use of multiple ion counters (MICs) extended the lower limit of detection with lower repeatability and intermediate precision because of the poorer linearity of MIC results in comparison to MFC results, in particular, with the early-stage miniature MIC devices.[10-13] Developments in MFC-ICPMS using a high efficiency ion sampling interface improved the sensitivity by about an order of magnitude.[10, 12, 14] Also, the sampling efficiency of LA has been approximately doubled by the use of UV femtosecond laser ablation (UVFsLA)[15] in place of UVNsLA. Present day sensitivity of the complete UVFsLA-MFC-ICPMS system has been reported to be >1% atom transmission from the LA crater to the Faraday collector, which rivals the ion transmission of typical thermal ionisation mass spectrometry (TIMS).[10]

Further advancement in MFC-ICPMS also has occurred through increases in the amplification gain of the Faraday circuit amplifiers. Conventional MFC-ICPMS (and TIMS) used amplifiers equipped with a 10^{11} Ω or a 10^{12} Ω resistor.[2, 8, 9, 16] Recently, a high gain Faraday amplifier with a 10^{13} Ω resistor (hereafter, 10^{13} Ω amplifier) has become available and applications in TIMS have been reported with high-precision isotope ratio determinations of small amounts of sample at the 10 pg level.[17-19] Application of 10^{12} Ω amplifiers to UVFsLA-MFC-ICPMS has been recently reported and the analytical accuracy (trueness and precision) compared favourably with that of SIMS using a single secondary electron multiplier (SEM; ion counter) for a 1.7 ppm Pb

glass sample (~1.5% 2 standard deviations: 2 SD) from a crater with 30 μm diameter and 30 μm depth. For samples with Pb > 10 ppm, the repeatability was much better (< 0.2% 2 SD) than that of SIMS.[2] Although the analytical repeatability was better in UVFsLA-MFC-ICPMS than in SIMS, approximately 5 times more sample was needed. This limits the application of UVFsLA-MFC-ICPMS to tiny glass samples such as olivine melt inclusions.[3, 16]

In this paper, we present the use of 10^{13} Ω amplifiers equipped with UVFs-MFC-ICPMS instrumentation for the analysis of ^{206}Pb-based Pb isotope ratios in small amounts of glass samples. The ^{204}Pb based isotope ratios are important in geochemical studies but achievable repeatability with LA-MFC-ICPMS (one to a few % 2 SE) is still far below than required[13, 16]. To eliminate the effect from ^{204}Hg interference, an approach other than improving sensitivity is needed, which is beyond the scope of this paper. Because of the slow response of the extremely high gain 10^{13} Ω amplifiers, particular care must be taken to achieve a precise and accurate analysis. We evaluated the properties of 10^{13} Ω amplifiers and improved the previously reported correction method for the slow response of 10^{11} Ω and 10^{12} Ω amplifiers.[20, 21] Gain calibration of the 10^{13} Ω amplifiers was not available on the instrument used and hence standard bracketing was used to correct for the gain factor of the amplifiers.[17-19] However, an accurate and easy gain calibration method for the 10^{13} Ω amplifiers was identified and examined, and details for this procedure are presented in this paper. Finally, the analytical repeatability, intermediate precision, and laboratory bias, measured by using glass standards were compared with those obtained by 10^{11} Ω amplifiers,[16] by 10^{12} Ω amplifiers,[2] and by MIC.[10] The results demonstrated the excellent performance of the 10^{13} Ω amplifiers when combined with a high sensitivity UVFsLA-MFC-ICPMS system.

2. Experimental

In this section, we provide fundamental information about the samples, instrumental setup, and data acquisition and correction.

2.1. Samples

We used synthetic standard reference material (SRM) glass samples SRM 610 and SRM 612 provided by the National Institute of Standards and Technology (NIST). The former contained 426 ppm Pb and the latter contained 38.57 ppm Pb in a silica-rich alumina–calcium–sodium glass matrix.[22, 23] Fused basalt glass standards BHVO-2G and BCR-2G provided by the United States Geological Survey (USGS), containing 1.7 ppm and 11 ppm Pb respectively, were also used as unknown samples.[22, 23] The isotopic composition of Pb in the glasses has been analysed by high-precision solution multiple collector-ICPMS (MC-ICPMS) methods by Baker *et al*. (2004)[24] for the NIST standards, and by Elburg *et al.* (2006)[25] for the USGS basalt glass standards.

2.2. Instrumental setup

The instrumentation and setup used for the UVFsLA and MFC-ICPMS are briefly described below. Details have been reported elsewhere for the UVFsLA[23] and MFC-ICPMS[16, 26] instruments.

2.2.1. Laser ablation. We used a 200/266 nm UVFsLA system (OK-Fs2000K, OK Laboratory, Tokyo, Japan), situated at the Japan Agency for Marine-Earth Science and Technology (JAMSTEC). The UVFsLA system uses a Solstice one-box Ti-sapphire femtosecond regenerative amplifier (Spectra-Physics, Santa Clara, CA, USA) with TP-1A THG (third harmonic generator) and TP-1A FHG (fourth harmonic generator) frequency tripling and quadrupling harmonic generators (Spectra-Physics, Santa Clara, CA, USA). Details of the instrument have been reported elsewhere.[23] The laser fluence on the sample surface was ~12 J cm^{-2} and ~6 J cm^{-2} for the 266 nm and 200 nm modes, respectively. For a normal operation, the rotating raster ablation protocol[23] was used with a 20 μm/25 Hz, 200 nm laser beam rastered along the circumference of a circle with 7 μm radius at a velocity of 7 μm s^{-1}, which resulted in a crater of size 30 μm diameter × ~30 μm depth after 35 s. The repetition rate of the laser was reduced to 20, 15, 10, 8, 6, 5, and 1 Hz whenever various smaller signals were required. A line raster with a 50 μm/10–1 Hz, 266 nm beam at a velocity of 7 μm s^{-1} was also used whenever stronger signals were required. Our earlier work did not detect any elemental fractionation with different wavelengths in the UVFsLA.[23] The settings of the UVFsLA system are summarized in **Table 1**.

2.2.2. Multiple Faraday collector ICPMS. The UVFsLA unit was coupled to a modified Neptune MFC-ICPMS (Thermo Scientific, Bremen, Germany) at JAMSTEC. Helium ablation gas (1.15 L min^{-1}) was mixed with Ar sample gas (~1.3 L min^{-1}) in a cylindrical mixing chamber with an inner volume of 70 cm^3, immediately before reaching the ICP torch.[15, 27] This signal smoothing device was requisite in order to minimize the effect of the slow response of the high gain 10^{13} Ω amplifiers (**section 3.1**). The MFC-ICPMS interface was modified by the addition of a high speed rotary pump for high ion transmission (**Table 1**).[16, 26] The JET-sampler and X-skimmer cones were used with the guard electrode (GE) on. This setting allowed for extremely high sensitivity (~3000 V ppm^{-1} Pb by using an Aridus desolvating nebulizer in solution mode).[14] With this setting, yields of oxide molecular ions were enormous for some elements, such as Ce, Th, and U,[16, 26] whereas almost no oxide ions were found for Pb, so that there would be no effect on the sensitivity of Pb. Also, no detectable oxide and hydroxide interferences were found on Pb isotopes.

We assigned ^{206}Pb, ^{207}Pb, and ^{208}Pb to the H1, H2, and H3 Faraday collectors with the 10^{13} Ω amplifiers, respectively, for the analyses unless otherwise noted. The remaining isotope peaks for ^{202}Hg, ^{203}Tl, ^{204}Pb, and ^{205}Tl at the L3 to axial Faradays were connected with amplifiers by using a 10^{12} Ω resistor for ^{202}Hg and ^{204}Pb and a 10^{11} Ω resistor for ^{203}Tl and ^{205}Tl. Sensitivity tuning and peak centring were performed by ablation of the SRM 612 standard by a line raster mode with a 50 μm/10 Hz, 266 nm laser beam moving at a velocity of 7 μm s^{-1}. The obtained signal intensity with this ablation mode was ~12–20 mV at the ^{208}Pb peak, corresponding to a sensitivity of 380,000–630,000 cps ppm^{-1} during ion counting. Peaks at ^{202}Hg, $^{204}Pb/^{204}Hg$, ^{203}Tl, ^{204}Pb, and ^{205}Tl were for monitoring only. The use of Tl external correction has been useful with solution ICPMS[28] but Tl is not always contained in unknown samples, which prevents use of this correction method in LA-MFC-ICPMS. The standard bracketing method properly corrects for mass bias even with different matrices,[8, 16] if corrections are made in short time intervals.[12] Details of the cup configuration and other settings of the MFC-ICPMS instrumentation are given in **Table 1**.

2.3. Data acquisition and correction

The high gain 10^{13} Ω amplifiers did not accept normal instrumental gain calibration.

Additionally, data acquisition required optimization to account for the slow response of the 10^{13} Ω amplifiers. In order to manage these problems, we examined gain calibration and data acquisition–correction procedures. The details are described below.

2.3.1. Amplifier gain calibration. Amplifier gain calibration is usually conducted with the mass spectrometer instrument, by application of an artificial 3.33333 V to all 10 amplifier boards. However, this method is not applicable to 10^{13} Ω amplifiers, perhaps because of their slow response. The conventional gain calibration was available for co-inserted 10^{11} Ω and 10^{12} Ω amplifiers, but this was skipped for the 10^{13} Ω amplifiers. In this study, we applied the standard bracketing method to determine Pb isotope ratios in unknown samples with all ^{206,207,208}Pb signals analysed by the 10^{13} Ω amplifiers (**Table 1**). In principle, therefore, gain calibration was not necessary. However, it is worth performing gain calibration because the measured raw data are, in practice, immediately comparable with those from the 10^{11} Ω or 10^{12} Ω amplifiers.

Gain calibration of the 10^{13} Ω amplifiers can be made by applying well-controlled ion signals while assuming that all the Faraday cup efficiencies are identical, which is almost always true. At least one amplifier with a 10^{11} Ω or a 10^{12} Ω resistor should be calibrated together with the three 10^{13} Ω amplifiers in order to correlate the gain factors of the 10^{13} Ω amplifiers to the rest of the amplifiers, because 10^{13} Ω amplifiers may be used together with the low gain amplifiers. We used ^{143}Nd, ^{144}Nd, and ^{146}Nd isotopes from a well-characterized Johnson Matthey Chemicals (JMC) standard solution that had an isotope ratio of ^{143}Nd/^{144}Nd = 0.512194 ± 0.000006 (2 standard errors: 2 SE), as determined by TIMS.[26]

Prior to gain calibration, we measured the JMC solution by using an Aridus solution aerosol–LA aerosol dual intake system equipped with MFC-ICPMS[26] instrumentation; this was accomplished by using 10^{11} Ω amplifiers with all three ^{143}Nd, ^{144}Nd, and ^{146}Nd isotopes after instrumental gain calibration of the amplifiers. The instrumental setup achieved a very low oxide yield of $Nd^+/NdO^+ < 0.001\%$, thus allowing for standardless determination of Nd isotopes.[26] The LA aerosol intake line (1.2 L min^{-1} He gas flow) was connected in order to achieve such a performance, but LA aerosols were not introduced. We obtained ^{143}Nd/^{144}Nd = 0.512211 ± 0.000070 (2 SE) for the JMC solution, which matched the TIMS value. We then operated the same system by switching amplifiers and using the relay matrix with a 10^{12} Ω amplifier (Amp

1) and three 10^{13} Ω amplifiers (Amps 2–4), and we applied the three Nd isotope signals to all the amplifiers with different amplifier–Faraday collector combinations (**Table 2**). The Nd isotope signals were set at < 200 mV at the largest peak of ^{144}Nd, to accommodate the high sensitivity of 10^{13} Ω amplifiers (see **section 3.2**).

Measured ^{143}Nd/^{144}Nd isotope ratios were normalized to ^{146}Nd/^{144}Nd = 0.7219 (ref.[29]) and corrected for mass fractionation by the exponential law[30-32] to obtain four isotope ratios, ^{143}Nd/^{144}Nd$_{meas_1–4}$, for the different collector–amplifier combinations (**Table 2**). The exponential law equations[32, 33] including amplifier gain factors AGF1–4 are expressed as Eqs. (1)–(4) below:

$$\frac{^{143}Nd}{^{144}Nd}_{calc\_1} = \left[\frac{^{143}Nd}{^{144}Nd}_{meas\_1} \times \left(\frac{AGF1}{AGF2}\right) \times \left(\frac{^{143}M}{^{144}M}\right)\right]^{\left\{\frac{\ln\left[\left(\frac{0.7129}{0.7129}\right)\times\left(\frac{AGF3}{AGF2}\right)\right]}{\ln\left(\frac{^{146}M}{^{144}M}\right)}\right\}} \quad (1)$$

$$\frac{^{143}Nd}{^{144}Nd}_{calc\_2} = \left[\frac{^{143}Nd}{^{144}Nd}_{meas\_2} \times \left(\frac{AGF2}{AGF3}\right) \times \left(\frac{^{143}M}{^{144}M}\right)\right]^{\left\{\frac{\ln\left[\left(\left(\frac{0.7129}{0.7129}\right)\right)\times\left(\frac{AGF4}{AGF3}\right)\right]}{\ln\left(\frac{^{146}M}{^{144}M}\right)}\right\}} \quad (2)$$

$$\frac{^{143}Nd}{^{144}Nd}_{calc\_3} = \left[\frac{^{143}Nd}{^{144}Nd}_{meas\_3} \times \left(\frac{AGF3}{AGF4}\right) \times \left(\frac{^{143}M}{^{144}M}\right)\right]^{\left\{\frac{\ln\left[\left(\left(\frac{0.7129}{0.7129}\right)\right)\times\left(\frac{AGF1}{AGF4}\right)\right]}{\ln\left(\frac{^{146}M}{^{144}M}\right)}\right\}} \quad (3)$$

$$\frac{^{143}Nd}{^{144}Nd}_{calc\_4} = \left[\frac{^{143}Nd}{^{144}Nd}_{meas\_4} \times \left(\frac{AGF4}{AGF1}\right) \times \left(\frac{^{143}M}{^{144}M}\right)\right]^{\left\{\frac{\ln\left[\left(\frac{0.7129}{0.7129}\right)\times\left(\frac{AGF2}{AGF1}\right)\right]}{\ln\left(\frac{^{146}M}{^{144}M}\right)}\right\}} \quad (4)$$

where atomic mass weights (^{143}M, ^{144}M, and ^{146}M) were obtained from the International Union of Pure and Applied Chemistry (IUPAC)[34] and 0.7129 was the normalization factor for ^{146}Nd/^{144}Nd (ref.[29]). The left side ^{143}Nd/^{144}Nd$_{calc_1–4}$ values were equal to the measured values ^{143}Nd/^{144}Nd$_{meas_1–4}$ when the amplifier gain factors AGF1–4 were all unity.

However, each amplifier had a different gain factor, so the measured isotope ratios ^{143}Nd/^{144}Nd$_{meas_1–4}$ were different (**Table 2**). Absolute differences in the isotope

ratios from the standard JMC solution were calculated by $D_{meas\_1–4} = {}^{143}Nd/{}^{144}Nd_{meas\_1–4} – 0.5122190$, and the total sum of the absolute differences $\sum D_{meas\_1-4}$ was obtained. By changing AGF1–4 values, the minimum value of $\sum D_{meas\_1-4}$ was found by using a non-linear solver function in an Excel spreadsheet containing Eqs. (1)–(4) and measured values of ${}^{143}Nd/{}^{144}Nd_{meas\_1–4}$. As a result, ${}^{143}Nd/{}^{144}Nd_{calc\_1–4}$ became close to 0.5122190 and the gain factors AGF1–4 were obtained.

Finally, the gain factors of the three 10^{13} Ω amplifiers were normalised to the gain factor of the 10^{12} Ω amplifier (Amp 1) that was determined in advance (or retrospectively) by the instrumental gain calibration procedure. Examples of the gain factors and the measured results of the JMC standard via the use of the three 10^{13} Ω amplifiers after gain calibration are shown in **Table 2**. The results showed almost perfect gain calibration, and this was confirmed by the JMC value of ${}^{143}Nd/{}^{144}Nd = 0.512210 \pm 0.000033$ (2 SE) after calibration, which was identical to the value of ${}^{143}Nd/{}^{144}Nd = 0.512211 \pm 0.000070$ (2 SE) measured before gain calibration with 10^{11} Ω amplifiers.

There are two caveats for this model. One is that the measured ${}^{143}Nd/{}^{144}Nd$ ratio of the standard solution should reflect the reference value. The MFC-ICPMS instrumentation will sometimes produce inaccurate ${}^{143}Nd/{}^{144}Nd$ ratios, dependent on instrumental settings, or with high oxide molecular yields.[26, 35, 36] Thus, instrumental settings should be optimized to reproduce the standard reference value. Alternatively, measured ${}^{143}Nd/{}^{144}Nd$ isotope ratios before gain calibration can be used for the target value in the solver calculations, and this value should be reproduced by measurements after gain calibration. The second caveat is to set the gain factor in the executive table for the MFC-ICPMS instrumentation to 1 for all Amps 1–4 (that is, 0.1 for Amp 1 with the 10^{12} Ω resistor and 0.01 for Amps 2–4 with 10^{13} Ω resistors in the case of Neptune) prior to the gain calibration for all 10^{12} Ω and 10^{13} Ω amplifiers. Without doing this, the solver calculations will involve these factors and the obtained gain factors will be incorrect.

2.3.2. Data acquisition. The slow response of the 10^{13} Ω amplifiers prevents accurate acquisition of the beam intensity from highly fluctuating LA signals.[20, 21] In particular, isotope ratios measured during signal ramp and decay are strongly affected.

Therefore, LA signals during the first 8 s were discarded by setting the Faraday amplifier idle time appropriately, and values for the flatter plateau region of LA signals were acquired before the LA was switched off to washout the aerosols (**Fig. 1a**). In order to closely monitor the variation in signal intensities during data acquisition (see **section 2.3.3** below), we set a ~0.5 s single scan time and acquired 34 scans for an analytical run of a laser crater (**Fig. 1a**).

2.3.3. Data correction. Figs. 1b and 1c show examples of the slow response of the 10^{13} Ω amplifiers against fluctuating LA signals, even in the flatter plateau region. The measured isotope ratios in a designated time interval ($[^{20X}Pb/^{206}Pb]/dt$) were compared with the rates of signal intensity change in the same time interval ($D^{208}Pbi/dt$). The changes were synchronous between the measured rates and the isotope ratios with a greater slow response effect in $[^{208}Pb/^{206}Pb]/dt$ than in $[^{207}Pb/^{206}Pb]/dt$. This was because the signal intensities in natural ^{208}Pb were about twice the quantities than in ^{206}Pb and ^{207}Pb (see **Fig. 2**, where $^{208}Pb/^{206}Pb$ = ~2.1 and $^{207}Pb/^{206}Pb$ = 0.9). The unstable signals from LA aerosols caused larger absolute deviations in the ^{208}Pb signals than those in the ^{206}Pb and ^{207}Pb signals. This resulted in a greater effect for the slow response of the amplifier assigned to ^{208}Pb.

The relationship between the rates of signal intensity change and isotope ratios in a designated time interval have been recognized and examined thoroughly in previous studies. These studies have shown that a linear correlation exists between the rates of signal intensity change ($D^{208}Pbi/dt$ in this study) and isotope ratios ($[^{20X}Pb/^{206}Pb]/dt$).[20, 21] Our results confirmed that the same correlation could be found within a single measurement run from a crater, as exemplified in **Figs. 1 and 2**. The measured deviations $[^{20X}Pb/^{206}Pb]/dt$ deviated around $D^{208}Pbi/dt$ = 0, thus indicating that the barycentric coordinates of the deviation correlated with the isotope ratios of the measured sample. This was confirmed by comparison of the mass fractionation-corrected isotope ratios using SRM 612 as the standard and measuring BCR-2G as the unknown. The correlation slope was steeper in $[^{208}Pb/^{206}Pb]/dt$–$D^{208}Pbi/dt$ plots (**Fig. 2a**) in contrast to the gentler slope in $[^{207}Pb/^{206}Pb]/dt$–$D^{208}Pbi/dt$ plots (**Fig. 2b**).

This relation was true in all the measurements, and this encouraged us to apply the $[^{20X}Pb/^{206}Pb]/dt$–$D^{208}Pbi/dt$ corrections to cancel out the effects of slow responses by

recalculating the measured isotope ratios with the linear correlation lines[20, 21] (arrows in **Figs. 2a and 2b** represent the effects of the correction calculations). With the corrections, the resultant analytical errors (repeatability) became smaller, *i.e.*, the values changed from 0.0047 to 0.0020 (2 SE) for $^{208}Pb/^{206}Pb$ and from 0.0025 to 0.0020 (2 SE) for $^{207}Pb/^{206}Pb$ (**Figs. 2c and 2d**). Moreover, the averages of the corrected isotope ratios were almost identical with those of the uncorrected average ratios (see the almost directly proportional regression lines in **Figs. 2c and 2d**). This again indicated that deviations of the signals occurred around the barycentric coordinates of the correlation line, representing the averaged isotope ratios equal to that of the samples.

3. Results and discussion

In this section, we evaluate the analytical results for Pb isotope measurements made by UVFsLA-MFC-ICPMS and discuss the correction method for the slow response. The analytical performance given by repeatability, intermediate precision, and laboratory bias is also presented.

3.1. Correction of the slow response

Correction of the slow response of the 10^{13} Ω amplifiers can be made by linear regression of the $[^{20X}Pb/^{206}Pb]/dt–D^{208}Pbi/dt$ values obtained from one analytical run, as shown in **section 2.3.3** (**Fig. 2**). Previous studies by Hirata *et al*. (2003)[20] and Iizuka *et al*. (2005)[21] used a constant correction factor determined from artificially deviated signals generated by different LA pulse repetition rates (*e.g.*, alterations between 10 Hz and 1 Hz ablation operations). This was to account for uncorrected "*tau correction*" factors originating from different responses between Faraday amplifiers, even after "*tau corrections*" were made on each amplifier. Pettke *et al*. (2011)[37] also used an empirical correction factor to cope with this, applying (1) the *stepping tau correction* by using a previous deviation step to estimate the tau factor in the correcting step, and (2) *quadratic tau correction* using smoothed model data in order to cope with the large and abrupt signal intensity changes. However, they still found incorrect "*tau correction*" even with the smoothed quadratic tau correction method.

As above, and in our data, there are still uncorrected slow responses between

amplifiers even after the damping (*"tau"*) factor corrections were made on each Faraday amplifier. This is clearly shown by the slopes of the linear regression lines in the [^{20X}Pb/^{206}Pb]/dt–D^{208}Pbi/dt plots, which varied significantly over the signal intensity range, especially in the low signal region (**Fig. 3**). Therefore correction of the slope fitting was required to be performed individually based on one single measurement dataset from a crater (34 scans, see an example in **Fig. 1**). Moreover, about 2 times larger ^{208}Pb signals than those from ^{206}Pb and ^{207}Pb resulted in a significant difference in the slope values (as illustrated by **Figs. 2a, 2b**, and **3)**, and the slope values differed between different amplifier combinations, thus indicating different slow response factors (data not shown).

The slope values were proportional when they were plotted against the averaged D^{208}Pbi/dt values or ^{208}Pbi signal intensities (**Fig. 3**). This means that the extent of signal deviation was almost proportional to the absolute change in the signal intensity in our instrument with the 10^{13} Ω amplifiers (**Table 1**). The relation was expressed by D^{208}Pbi/dt = 0.0142 ± 0.0040 × ^{208}Pbi, thereby showing a ~1.4% absolute signal deviation of the total signal intensity. This is interesting, because observations showed that the slow response of the amplifiers depends either on the absolute rate of the signal change or on the difference in relative signal intensities applied to the different amplifiers. These observations further supported the application of the slow response corrections to the individual dataset from a single crater because Pb isotope ratios and Pb signals naturally varied between samples and between samples and standards.

From **Fig. 3**, we observed that one more aspect is possibly based on the relationship between the slope factor and D^{208}Pbi/dt or ^{208}Pbi. The largest slope value occurred when the absolute change in signals was small, in other words, when the signal intensity was small. In this particular case, deviations from the slow response were within the noise level of the measurement errors so that no correlation was generated, which resulted in a flat correlation line (a large absolute slope value). Measurement errors originating from ^{208}Pbi (abscissa of **Fig. 3**) can be described simply by the square root of the signal intensity ($N = \sqrt{n}$, where n is the signal intensity; more details regarding the errors are provided in **section 3.2**). Slow responses represented by the correlation slope (vertical axis of **Fig. 3**) may be simulated by the damping behaviour of

a kinematic spring–dashpot system described by the following function: $\zeta = c/\sqrt{mk}$, where m is the mass of weight, k is the spring constant, and c is the damping coefficient; that is, we assume an angular frequency dependent impedance of a resistor (R)–capacitor (C) circuit of the Faraday amplifier as the spring–dashpot system. When the N and ζ values were plotted against each other, square root terms were cancelled out and an asymptotic relation was generated. In fact, the examples in **Fig. 3** showed correlations represented by equation $y = -0.1 / x$ for $^{207}Pb/^{206}Pb$ and $y = -0.9 / x$ for $^{207}Pb/^{206}Pb$.

The above formulations could have been applied to estimate the slope values from the measured $D^{208}Pbi/dt$ or ^{208}Pbi values for a given combination of the 10^{13} Ω amplifiers. However, conditions may have differed via long-term changes in the conditions of the amplifiers or short-term changes in the LA conditions, *i.e.*, changes in the isotope ratios or element abundance between craters. We therefore applied crater-by-crater corrections throughout this study by using the method shown in **Fig. 2**. To accomplish this, we generated an Excel spreadsheet and corrected the time resolved data off-line (**Figs. 1 and 2**). Corrections were made on the individual unknowns and the standard datasets were measured before and after the unknowns. The standard bracketing mass fractionation corrections were then made on the corrected values (**†ESI Data Tables 1 and 2**). In addition, error propagation between two bracketing standards and a bracketed unknown was calculated using an Excel matrix.[39]

This correction strategy did not depend on the element abundances and isotope ratios, which may have differed between the standards and the unknowns. Also, intentional changes in the laser sampling volume made by changes in the LA mode (20 μm diameter when using 200 nm wavelength at ~6 J cm^{-2} fluence and 50 μm diameter when using 266 nm wavelength at ~12 J cm^{-2} fluence), or by changes in the repetition rate of LA at different LA modes (1–25 Hz), did not affect the slope corrections (**†ESI Data Table 1**). Consequently, this method provided a proper correction for the slow response against various sources of disturbances such as those from the sample and the ablation conditions and others from the amplifiers including the Faraday–amplifier assignment and long-term drifts of the amplifiers.

An alternative correction method would be a bulk signal integration.[37] This can

be applied by the observations in the deviations of the signals which occurred around the barycentric coordinates representing the averaged isotope ratios equal to that of the samples (**Fig. 2**, **section 2.3.3**). We also applied the bulk signal integration approach with MICs for Os isotope analysis using a sparging method.[38] However, analytical errors can only be estimated by the counting statistics for analysis of a single crater. As such, the error calculation cannot reflect changes in isotope ratios and signal intensities during ablation of a single crater (see above). This is a disadvantage of micro analysis, and so we do not apply this method.

3.2. Repeatability of the Pb isotope analysis

With the correction method proposed above, we analysed glass standards SRM 610 (426 ppm Pb), SRM 612 (38.57 ppm), BCR-2G (11 ppm), and BHVO-2G (1.7 ppm)[22, 23] with various LA intensities by using both the 266 nm and 200 nm laser ablation modes; the aim was to evaluate the repeatability achieved by the UVFsLA-MFC-ICPMS instrumentation with high gain 10^{13} Ω amplifiers (see LA conditions in **Table 1**). Measured signal intensities ranged from 0.1–300 mV at the largest ^{208}Pbi signal (**†ESI Data Table 1** and **Fig. 4**).

Our research team measured Pb isotopes in the same glass standards by using the same high sensitivity MFC-ICPMS instrumentation (**Table 1**) with the Faraday collectors and the 10^{11} Ω and 10^{12} Ω amplifiers[2, 16]; miniature MICs were also used.[10] These analytical results are plotted in **Figs. 4a and 4b,** together with the data obtained in this study through the use of 10^{13} Ω amplifiers. The repeatability obtained by the 10^{11} Ω amplifiers ranged from 0.1–0.01% 2 SE for the signal intensity range of 50–300 mV at ^{208}Pbi. Those obtained by the 10^{11} Ω amplifiers were 2–0.05% 2 SE for the signal intensity range of 2–100 mV (**Fig. 4a**). All the relationships between ^{208}Pbi and % 2 SE were linear in log–log space and formed linear arrays (**Fig. 4a**).

The MIC analyses used three miniature MICs for the three Pb isotopes. Statistical features almost followed the theoretical values, which were calculated by Eqs. (5)–(8) as follows:

$$I^{^{20X}Pb} = I^{^{20X}Pb} - BG^{20X} \quad (X = 6, 7, 8) \tag{5}$$

$$\left(\sigma_{I^{20X_{Pb}}}\right)^2 = (\sigma_{I^{20X}})^2 + \left(\sigma_{BG^{20X}}\right)^2 \quad (6)$$

$$\%\sigma_{20X/206_{Pb}} = \frac{I^{20X_{Pb}}}{I^{206_{Pb}}} \times \sqrt{\left(\frac{\sigma^{20X_{Pb}}}{I^{20X_{Pb}}} \times 100\right)^2 + \left(\frac{\sigma^{206_{Pb}}}{I^{206_{Pb}}} \times 100\right)^2}$$

$$(X = 7, 8) \quad (7)$$

$$\%SE_{20X/206_{Pb}} = \frac{\%\sigma_{20X/206_{Pb}}}{\sqrt{n}} \qquad (X = 7, 8) \quad (8)$$

where ^{20X}Pb is the intensity (cps) of the Pb ion beam, *BG* is the baseline intensity (cps), *I* is the intensity of the bulk ion beam, σ is the standard deviation of the beam intensity or isotope ratios, % SE is the percent standard error of the measured Pb isotope ratios, and *n* is total scan number; in the signal range of 10–800 kcps, this yielded 0.1–0.6 % 2 SE (see the counting statistics line in **Figs. 4a and 4b**).[10]

The relationship between the analytical errors and the signal intensities when using 10^{11} Ω, 10^{12} Ω, and 10^{13} Ω amplifiers has been reported by TIMS.[18, 40] The measured % 2 SE values in $^{87}Sr/^{86}Sr$ and $^{143}Nd/^{144}Nd$ by 10^{13} Ω amplifiers were around a factor of 2 worse than that of counting statistics in ion counters in the 1–100 mV range. The errors by 10^{12} Ω and 10^{11} Ω amplifiers were 3 and 5 times greater than those by 10^{13} Ω amplifiers (see star symbols in **Fig. 4b**). In contrast to our UVFsLA measurements, errors in TIMS were about a factor of 2–3 times smaller for all the different amplifiers (**Fig. 4b**). The TIMS analyses were made by sufficiently long acquisition times of 11 min (660 times for 1 s measurements) in both baseline and signal measurements.[18, 40]

The TIMS analyses confirmed that the absolute baseline noise of ~1.4 μV was comparable with the Johnson–Nyquist noise level (Eq. 9); with the calculation as follows:

$$\Delta V = \sqrt{\frac{4k_B RT}{t_m}} \quad (9)$$

where ΔV is the 1 SD noise in volts, k_B is the Boltzmann constant, *R* is the resistor

impedance in Ω, T is the temperature in Kelvin, and t_m is the integration time in seconds (frequency, in Hz), which was calculated as ΔV = ~1.6 μV with a 10^{11} Ω impedance, 0.0015 Hz frequency band (660 s scan time), and ~37 °C (~310 K) amplifier temperature.[41] This thermal noise is regarded to be the major source of errors in Faraday amplifier circuits.[18, 40] Researchers[17,36] have reported that 10^{12} Ω and 10^{13} Ω amplifiers had average noise levels of ~0.8 μV and 0.3 μV (1 SE) after being corrected for the 10 and 100 times higher gains relative to the 10^{11} Ω amplifiers; these noise levels represent an improvement by a factor of 1.8 and 5, respectively, compared to the 10^{11} Ω amplifiers, but were approximately 2 times worse than the theoretical improvements of the signal to noise ratios (S/N), which were increased by factors of 3 and 10, respectively.[18, 40]

With Eqs. (5)–(9), the % SE errors for Pb isotope analysis while using Faraday collectors were formulated as Eqs. (10)–(14) as follows:

$$\sigma_{JN} = \Delta\mathrm{V} \div 100 \tag{10}$$

$$I^{^{20X}Pb} = I^{^{20X}Pb} - BG^{20X} \quad (X = 6, 7, 8) \tag{11}$$

$$I_{^{20X}Pb} = I_{^{208}Pb} \times R_{^{20X}Pb/^{208}Pb} \qquad (X = 6, 7, 8) \tag{12}$$

$$\%\sigma_{^{20X}Pb/^{206}Pb} = \sqrt{\left(\frac{\sigma_{JN}}{I^{^{20X}Pb}} \times 100\right)^2 + \left(\frac{\sigma_{JN}}{I^{^{206}Pb}} \times 100\right)^2} \quad (X = 7, 8) \tag{13}$$

$$\%SE_{^{20X/206}Pb} = \frac{\%\sigma_{^{20X/206}Pb}}{\sqrt{n}} \qquad (X = 7, 8) \tag{14}$$

where σ_{JN} is obtained from 1 SD of the Johnson–Nyquist noise (ΔV in mV), I is the bulk intensity of the ion beam (mV), BG is the baseline intensity (mV), R is the isotope ratios, % SE is the percent standard error of the measured Pb isotope ratios, and n is the scan number in an analysis.

Overall, the repeatability achieved by the 10^{13} Ω amplifiers in this study was 1–0.04% 2 SE in the signal intensity range for ^{208}Pbi of 1–100 mV (**Fig. 4b**). The variations of the measured % 2 SE errors were reproduced by the calculated errors of Eq. (14) when the Johnson–Nyquist noise was assumed to be 20 μV. This noise level was

more than 30 times higher than the measured value in TIMS (~0.6 μV) when using 10^{13} Ω amplifiers.[18] The analytical errors obtained in this study and our previous studies[2, 10, 15] were from a very short acquisition time of 60 s (2 cycles of 30 s scans, **Table 1**) in contrast to the sufficiently long acquisitions (660 cycles of ~1 s scans) made by TIMS.[18, 40] This was because of the baselines used in this study, which stand for on-peak backgrounds (**Table 1**) due to presence of the cone memories in all ^{206,207,208}Pb isotope peaks.

The extremely high sensitivity of the modified MFC-ICPMS procedure led to the detection of the cone memory signals at the 800–1500 μV level. This far exceeded that of the theoretical Johnson–Nyquist noise (1 SD), which was ~0.2 μV for the 10^{13} Ω amplifiers (recalculated to 10^{11} Ω amplifier equivalents) at the analytical conditions given above, and it shared 80–90% of the total Pb signals for the lowest quantity Pb sample analysed in this study (~150 μV ^{208}Pbi, see **Fig. 4b**). However, considering the difficulties with these conditions, baseline stability with UVFsLA-MFC-ICPMS was excellent. The estimated 1 SD Johnson–Nyquist noise of 20 μV from the observed % 2 SE errors was small enough for such high baselines. This was actually confirmed by the 1 SD errors measured by the blank baseline analyses after on-peak baseline subtraction, which yielded 20 ± 5 μV (error in 1 SD, n = 16, data not shown) and was perfectly comparable with that of the assumed noise level of 20 μV.

The measured (and theoretical) ^{208}Pbi–% 2 SE slope obtained by UVFsLA-MFC-ICPMS when using 10^{13} Ω amplifiers was sub-parallel to that obtained by the 10^{11} Ω and 10^{12} Ω amplifiers and was about 2–3 times better in the 1–50 mV signal intensity range. The simulated Johnson–Nyquist noise error was ~60 μV for 10^{12} Ω amplifiers, which was about 3 times worse in terms of the S/N than that with the 10^{13} Ω amplifiers (**Fig. 4a and 4b**). The relative improvement in the analytical repeatability by using the 10^{13} Ω amplifiers over the 10^{11} Ω and 10^{12} Ω amplifiers was comparable with that found in TIMS.[18] The repeatability was poorer than the theoretical errors in signal intensities higher than 50 mV, and it overlapped with those obtained by use of the 10^{11} Ω and 10^{12} Ω amplifiers. Further, the repeatability was inferior in the intensity range higher than 200 mV (20 V equivalents in 10^{11} Ω amplifiers), thus indicating the presence an upper signal limit for the 10^{13} Ω amplifiers (**Fig. 4a and 4b**).[18]

Conclusively, the above comparisons showed that the analytical performance of

the 10^{13} Ω amplifiers was superior to that of the 10^{11} Ω and 10^{12} Ω amplifiers in the signal range 1–100 mV and the repeatability of the data was about 2–3 times better. The repeatability when using the 10^{13} Ω amplifiers was still good enough at the signal level down to 0.3 mV, if the 3% 2 SE error was acceptable. The upper signal limit was about 200 mV, at which inferior repeatability with 10^{12} Ω amplifiers became obvious (**Fig. 4b**).

Meanwhile, repeatability by the miniature MIC was about a factor of 2–10 better than that by the 10^{13} Ω amplifiers in the signal range 0.1–8 mV; the repeatability overlapped at around 10 mV (~7000 kcps, **Fig. 4b**), which was the approximate linearity limit of the miniature MIC.[10] The repeatability of the MIC was apparently superior in the signal range 0.1–7 mV; however, this did not guarantee high intermediate precision and low laboratory bias, which will be discussed next in **section 3.3**.

3.3. Laboratory bias and intermediate precision of the Pb isotope analysis

Evaluation of the laboratory bias was conducted by analysing the BHVO-2G (1.7 ppm Pb) and BCR-2G (11 ppm Pb) basalt standard glasses as unknowns and by using the SRM 612 (38.57 ppm Pb) standard glass as a standard. Crater-by-crater corrections of the slow response were made and standard–sample–standard bracketing and error propagation calculations were performed on the corrected values. The results are shown in **†ESI Data Table 1, Table 3, and Fig. 5.**

The laboratory bias of the $^{208}Pb/^{206}Pb$ and $^{207}Pb/^{206}Pb$ isotope ratios in BHVO-2G and BCR-2G basalt glass samples was ±0.05–0.15 ‰ RD (‰ relative difference) from the solution MFC-ICPMS values,[25] and the intermediate precision was ±3–7 ‰ 2 SD for BHVO-2G and ±0.6–3.7 ‰ 2 SD for BCR-2G (**Table 3** and **Fig. 5**). The % 2 SD intermediate precision of BHVO-2G analysed by MIC were about twice as large as that by 10^{13} Ω amplifiers although the repeatability by MIC was far better (**Fig. 4a**). This was due to the large deviations of the analysed ratios between craters by MIC that were reflective of instabilities originating from the non-linearity within one MIC and between multiple MICs.[10-12] This problem persisted even with large SEM values; nevertheless, the extent was smaller than that with MIC.[8, 9]

In contrast to the ion counters, the high gain 10^{13} Ω amplifiers enabled very

accurate determinations of the Pb isotope ratios. The most remarkable results were shown by the ‰ 2 SD intermediate precision that were calculated by using the daily averages of BHVO-2G, where $^{208}Pb/^{207}Pb$ = 2.0477 ± 0.0032 (1.6‰ 2 SD) and $^{206}Pb/^{207}Pb$ = 0.8331 ± 0.0005 (0.6‰ 2 SD), and of BCR-2G, where $^{208}Pb/^{207}Pb$ = 2.0632 ± 0.0015 (0.7‰ 2 SD) and $^{206}Pb/^{207}Pb$ = 0.8322 ± 0.0003 (0.4‰ 2 SD) (**Table 3**). Such high intermediate precision was achieved only by the stable and high S/N ratio of the high gain 10^{13} Ω amplifiers (**Fig. 4b**). As a result, the laboratory bias obtained for the two basalt standards was ±0.05–0.15‰ RD, which almost rivals those by solution MFC-ICPMS.[25, 28] A comparable laboratory bias was possible with the 10^{12} Ω amplifiers, but the intermediate precision (and repeatability) was less, *i.e.*, twice as large in terms of ‰ 2 SD than those by 10^{13} Ω amplifiers (**Fig. 5**). This was more apparent in the low signal region < 50 mV (**Fig. 4b**).

Overall, the performance of the 10^{13} Ω amplifiers was excellent and showed advantages over MIC and over 10^{11} Ω and 10^{12} Ω amplifiers. Achievable repeatability from craters with 30 μm diameters and 30 μm depths were better than 1.9‰ 2 SD from in $^{208}Pb/^{206}Pb$ from 1.7 ppm Pb (BHVO-2G) and 1.2‰ 2 SD from 11 ppm Pb (BCR-2G) glass samples. A similar measurement using a 193 nm excimer LA and MFC-ICPMS with crater diameters of 23 and 45 μm, with an acquisition time of 30 s, achieved 6‰ 2 SD (n = 20) and 2.7‰ 2 SD (n = 116), respectively, in $^{208}Pb/^{206}Pb$ from BHVO-2G (data from Tables 4 and 6 in Zhang *et al.*, 2014).[13] Our result from a crater diameter of 30 μm with an acquisition time of 15 s was 1.9‰ 2 SD (n = 20) using 10^{13} Ω amplifiers (**Table 3**). The improvement in this study was simply due to the use of 10^{13} Ω amplifiers.

These precisions were more than an order of magnitude smaller than those by SIMS,[4, 7] although the consumed sample amount was about 5 times larger than that by SIMS, which uses crater depths of only ~5 μm and crater diameters of <30 μm. Nevertheless, if a repetition rate of 5 Hz was used in UVFs-MFC-ICPMS, obtained repeatability was 1.5% 2 SE for BHVO-2G and 0.3% 2 SE for BCR-2G from the same crater size as LA (**†ESI Data Table 2**). These were comparable with those by SIMS.[23] The high sensitivity accomplished by the high efficiency interface vacuum pump with JET–X high transmission sample–skimmer cones,[14, 16] together with the use of the high gain 10^{13} Ω amplifiers[18, 19] ultimately brought up the sensitivity of

UVFsLA-MFC-ICPMS to a level that was comparable with that of SIMS. Better repeatability and intermediate precision were also accomplished with a greater sampling volume; this was easily achievable by UVFsLA-MFC-ICPMS given the excellent linearity and S/N of the 10^{13} Ω amplifiers. These performance attributes and operational flexibilities will open up new application fields for the microanalysis of Pb isotopes in tiny amounts of glass and low-content Pb mineral samples.

4. Conclusions

We presented analytical results for $^{208}Pb/^{206}Pb$ and $^{207}Pb/^{206}Pb$ isotope analyses of BHVO-2G and BCR-2G basalt glass samples, containing 1.7 ppm and 11 ppm Pb respectively, that were obtained by using UVFsLA-MFC-ICPMS instrumentation equipped with three state-of-the-art high gain 10^{13} Ω amplifiers. The slow response of the 10^{13} Ω amplifiers was corrected for by employing the $[^{20X}Pb/^{206}Pb]/dt–D^{208}Pbi/dt$ relationship obtained from analytical data on a single crater. This approach improved the repeatability by compensating for the different slow response factors between the 10^{13} Ω amplifiers. Obtained laboratory bias and intermediate precisions, after standard bracketing mass fractionation correction using SRM 612 standard glass as an external standard, were ±0.05–0.15‰ RD for both glasses and ±3–7‰ 2 SE for BHVO-2G and ±0.6–3.7‰ 2 SE for BCR-2G. These were approximately 2–3 times better than those obtained by either MIC-ICPMS or by MFC-ICPMS with 10^{12} Ω amplifiers. The extra-high sensitivity of the present system also enabled comparable analytical performance with SIMS (2–0.5% 2 SE) from the same sample size.

Acknowledgments

Our thanks go to Dr C. Bouman of Thermo Scientific for technical assistance and Prof. T. Hirata of Kyoto University for valuable discussions. Comments from three anonymous reviewers greatly helped to improve the manuscript. J.-I.K. was funded by the Japan Society for the Promotion of Science (JSPS) (grant 15H02148).

References

1. A. J. R. Kent, M. C. Rowe, J. Pallister and C. R. Thornber, in *A volcano rekindled; the renewed eruption of Mount St. Helens, 2004-2006, U.S. Geological Survey Professional Paper 1750*, ed. D. R. Sherrod, W. E. Scott and P. H. Stauffer. 2008, vol. 1750, pp. 809-826.
2. J.-I. Kimura, Y. Nagahashi, Y. Satoguchi and Q. Chang, *Geochemistry, Geophysics, Geosystems*, 2015, **16**, 2147-2174. DOI: 10.1002/2015gc005854.
3. B. Paul, J. D. Woodhead, J. Hergt, L. Danyushevsky, T. Kunihiro and E. Nakamura, *Chemical Geology*, 2011, **289**, 210-223. DOI: 10.1016/j.chemgeo.2011.08.005.
4. A. E. Saal, S. R. Hart, N. Shimizu, E. H. Hauri, G. D. Layne and J. M. Eiler, *Earth and Planetary Science Letters*, 2005, **240**, 605-620. DOI: 10.1016/j.epsl.2005.10.002.
5. E. Todd, A. Stracke and E. E. Scherer, *Geochemistry, Geophysics, Geosystems*, 2015, **16**, 2276-2302. DOI: 10.1002/2015gc005804.
6. D. Weis, B. Kieffer, C. Maerschalk, J. Barling, J. de Jong, G. A. Williams, D. Hanano, W. Pretorius, N. Mattielli, J. S. Scoates, A. Goolaerts, R. M. Friedman and J. B. Mahoney, *Geochemistry Geophysics Geosystems*, 2006, **7**, doi:10.1029/2006gc001283. DOI: 10.1029/2006gc001283.
7. A. E. Saal, S. R. Hart, N. Shimizu, E. H. Hauri and G. D. Layne, *Science*, 1998, **282**, 1481-1484. DOI: 10.1126/science.282.5393.1481.
8. A. J. R. Kent, *Journal of Analytical Atomic Spectrometry*, 2008, **23**, 968-975. DOI: 10.1039/b801046c.
9. B. Paul, J. D. Woodhead and J. Hergt, *Journal of Analytical Atomic Spectrometry*, 2005, **20**, 1350-1357. DOI: 10.1039/b507647a.
10. Q. Chang, J. I. Kimura, T. Miyazaki, S. Sasaki and N. Kanazawa, *Geochemical Journal*, 2014, **48**, 309-320. DOI: 10.2343/geochemj.2.0307.
11. A. Cocherie, C. M. Fanning, P. Jezequel and M. Robert, *Geochimica Et Cosmochimica Acta*, 2009, **73**, 1095-1108. DOI: 10.1016/j.gca.2008.11.028.
12. J.-I. Kimura, Q. Chang, K. Itano, T. Iizuka, S. B. Vaglarov and K. Tani, *Journal of Analytical Atomic Spectrometry*, 2014, **30**, 404-505. DOI: 10.1039/C4JA00257A.
13. L. Zhang, Z.-Y. Ren, A. R. L. Nichols, Y.-H. Zhang, Y. Zhang, S.-P. Qian and J.-Q. Liu, *Journal of Analytical Atomic Spectrometry*, 2014, **29**, 1393-1405. DOI: 10.1039/c4ja00088a.
14. C. Bouman, M. Deerberg, J. B. Schwieters and T. F. Scientific, *Application Note of Thermo Fischer Scientific*, 2008, **30187**, 1-4.
15. J.-I. Kimura, Q. Chang and K. Tani, *Geochemical Journal*, 2011, **45**, 283-296.
16. J.-I. Kimura, H. Kawabata, Q. Chang, T. Miyazaki and T. Hanyu, *Geochemical Journal*, 2013, **47**, 369-384.
17. M. Klaver, R. J. Smeets, J. M. Koornneef, G. R. Davies and P. Z. Vroon, *Journal of Analytical Atomic Spectrometry*, 2015. DOI: 10.1039/c5ja00130g.
18. J. M. Koornneef, C. Bouman, J. B. Schwieters and G. R. Davies, *Analytica Chimica Acta*, 2014, **819**, 49-55. DOI: 10.1016/j.aca.2014.02.007.
19. J. M. Koornneef, I. Nikogosian, M. J. van Bergen, R. J. Smeets, C. Bouman and G. R. Davies, *Chemical Geology*, 2015, **397**, 14-23. DOI: 10.1016/j.chemgeo.2015.01.005.
20. T. Hirata, Y. Hayano and T. Ohno, *Journal of Analytical Atomic Spectrometry*, 2003, **18**, 1283-1288. DOI: 10.1039/b305127g.

21. T. Iizuka, S. M. Eggins, M. T. McCulloch, L. P. J. Kinsley and G. E. Mortime, *Chemical Geology*, 2011, **282**, 45-57. DOI: 10.1016/j.chemgeo.2011.01.008.
22. K. P. Jochum, U. Nohl, K. Herwig, E. Lammel, B. Stoll and A. W. Hofmann, *Geostandards and Geoanalytical Research*, 2005, **29**, 333-338.
23. J. I. Kimua and Q. Chang, *Journal of Analytical Atomic Spectrometry*, 2012, **27**, 1549-1559. DOI: 10.1039/c2ja10344c.
24. J. Baker, D. Peate, T. E. Waight and M. F. Thirlwall, *Chemical Geology*, 2005, **217**, 175-179. DOI: 10.1016/j.chemgeo.2004.12.002.
25. M. Elburg, P. Z. Vroon, B. van der Wagt and A. Tchalikian, *Chemical Geology*, 2005, **223**, 196-207. DOI: 10.1016/j.chemgeo.2005.07.001.
26. J.-I. Kimura, Q. Chang and H. Kawabata, *Journal of Analytical Atomic Spectrometry*, 2013, **28**, 1522-1529. DOI: 10.1039/c3ja50109d.
27. J.-I. Kimura, K. Tani and Q. Chang, *Geochemical Journal*, 2012, **46**, 1-12.
28. J. Barling and D. Weis, *Journal of Analytical Atomic Spectrometry*, 2008, **23**, 1017-1025.
29. R. K. O'Nions, P. J. Hamilton and N. M. Evensen, *Earth and Planetary Science Letters*, 1977, **34**, 13-22. DOI: 10.1016/0012-821X(77)90100-5.
30. A. N. Halliday, D. C. Lee, J. N. Christensen, A. J. Walder, P. A. Freedman, C. E. Jones, C. M. Hall, W. Yi and D. Teagle, *International Journal of Mass Spectrometry and Ion Processes*, 1995, **146**, 21-33. DOI: 10.1016/0168-1176(95)04200-5.
31. T. Hirata, *Analyst*, 1996, **121**, 1407-1411.
32. M. F. Thirlwall and R. Anczkiewicz, *International Journal of Mass Spectrometry*, 2004, **235**, 59-81. DOI: 10.1016/j.ijms.2004.04.002.
33. N.-C. Chu, R. N. Taylor, V. Chavagnac, R. W. Nesbitt, R. M. Boella, J. A. Milton, C. R. German, G. Bayon and K. Burton, *Journal of Analytical Atomic Spectrometry*, 2002, **17**, 1567-1574. DOI: 10.1039/b206707b.
34. International_Union_of_Pure_and_Applied_Chemistry, *Pure and Applied Chemistry*, 1984, **56**, 695-768.
35. K. Newman, *Journal of Analytical Atomic Spectrometry*, 2011, **27**, 63-70. DOI: 10.1039/c1ja10222b.
36. K. Newman, P. A. Freedman, J. Williams, N. S. Belshawb and A. N. Halliday, *Journal of Analytical Atomic Spectrometry*, 2009, **24**, 742-751.
37. T. Pettke, F. Oberli, A. Audetat, U. Wiechert, C. R. Harris and C. A. Heinrich, *Journal of Analytical Atomic Spectrometry*, 2011, **26**, 475-492. DOI: 10.1039/c0ja00140f.
38. T. Nozaki, K. Suzuki, G. Ravizza, J.-I. Kimura and Q. Chang, *Geostandards and Geoanalytical Research*, 2012, **36**, 131-148. DOI: 10.1111/j.1751-908X.2011.00125.x.
39. J. Kragten, *Analyst*, 1994, **119**, 2161-2165. DOI: 10.1039/AN9941902161.
40. J. M. Koornneef, C. Bouman, J. B. Schwieters and G. R. Davies, *Journal of Analytical Atomic Spectrometry*, 2013, **28**, 749-754. DOI: 10.1039/c3ja30326h.
41. J. M. Koornneef, C. Bouman, J. B. Schwieters and G. R. Davies, *Analytica Chimica Acta*, 2014, **819**, 49-55.

694

Figure and table captions

Fig. 1 Changes in the signal intensity at ^{208}Pb (a) and changes in the rate of signal intensity (D^{20X}Pbi/dt) and measured Pb isotope ratios ([^{20X}Pb/^{206}Pb]/dt) within designated time intervals (b and c) that were analysed from a 30 μm diameter and 30 μm deep crater dug on an SRM612 standard glass sample.

Fig. 2 Correlations between the change in the rate of signal intensity (D^{20X}Pbi/dt) and measured Pb isotope ratios ([^{20X}Pb/^{206}Pb]/dt) within designated time intervals that were analysed from a 30 μm diameter and 30 μm deep crater dug on a BCR-2G standard glass sample (panels a and b). Panels c and d show results for slow response correction, before ([^{20X}Pb/^{206}Pb]/dt raw) and after ([^{20X}Pb/^{206}Pb]/dt corr.) the corrections. Errors, as indicated by 2 standard errors (2 SE), were reduced after corrections. Arrows in panels a and b show the corrections of the correlation slopes generated by the different slow responses of the assigned 10^{13} Ω amplifiers.

Fig. 3 Correlations between slope values from D^{20X}Pbi/dt–[^{20X}Pb/^{206}Pb]/dt plots and the change in the rate of signal intensity (D^{208}Pbi/dt) or absolute signal intensity (^{208}Pbi). Two asymptotic curves are shown by different isotope ratios for ^{208}Pb/^{206}Pb (open symbols) and ^{207}Pb/^{206}Pb (solid symbols). These were from different response of the amplifiers and different isotope ratios between ^{208}Pb/^{206}Pb and ^{207}Pb/^{206}Pb. D^{208}Pbi/dt and ^{208}Pbi/dt proportionally varied during laser ablation, thus indicating that the rate of signal fluctuation was almost constant but with different absolute values dependent on the signal intensities. See details in the text.

Fig. 4 Repeatability obtained from glass standard samples analysed by UVFsLA-MFC-ICPMS using 10^{11} Ω amplifiers[15], 10^{12} Ω amplifiers,[2] and MIC[10] (panel a) and using 10^{13} Ω amplifiers (panel b). Results from TIMS during the use of 10^{11} Ω, 10^{12} Ω, and 10^{13} Ω amplifiers[40, 41] are also shown by stars (panel b). Theoretical errors are shown for counting statistics for MIC (thin line) and for Johnson–Nyquist noise at 20 μV and 60 μV for 10^{13} Ω and 10^{12} Ω amplifiers, respectively (grey thick solid and dotted lines for ^{208}Pb/^{208}Pb (upper) and ^{208}Pb/^{208}Pb (lower)). Repeatability is shown by

the percentage for 2 standard errors (% 2 SE). The abscissa shows the averaged signal intensity measured at ^{208}Pb in mV (lower) and in kcps (upper).

Fig. 5 Analytical results of ^{208}Pb/^{206}Pb and ^{207}Pb/^{206}Pb isotope ratios for BHVO-2G and BCR-2G basalt glass samples (panels a and b). Each data point shows a single spot (30 μm diameter and depth) that was analysed by bracketing analysis with the SRM612 glass standard; errors are given as 2 standard errors (2 SE). Av.: daily average of five individual spots with 2 standard deviations (2 SD); GAv.: grand average using all individual spot data with 2 SD; MIC: analysis by using the MIC with 2 SD;[10] 10^{12} amps: analysis by using 10^{12} Ω amplifiers with 2 SD;[2] Ref.: reference values reported for solution ICPMS with 2 SE.[25] Averages and 2 SD values given by the daily averages are shown in Table 3.

Table 1 Laser and mass spectrometer setup parameters for UVFsLA-MFC-ICPMS

Table 2 Configurations of the Faraday amplifier combinations used for gain calibration

Table 3 Representative analytical results for Pb isotope ratios in BHVO-2G and BCR-2G basalt glasses

Electronic supplementary information (ESI) Data Table 1: Representative analytical precisions of Pb isotope ratios obtained by using 200FsLA-MFC-ICPMS with 10^{13} Ω resistor Faraday amplifiers

Electronic supplementary information (ESI) Data Table 2: Representative analytical results for Pb isotope ratios obtained by using 200FsLA-MFC-ICPMS with 10^{13} Ω resistor Faraday amplifiers

Table 1 Laser and mass spectrometer setup parameters for the UVFsLA-MFC-ICPMS[a]

Apparatus	Experimental setting	
[Femtosecond laser ablation system]		
Equipment	OK-Fs2000K OK Laboratory Ltd. (in house development)	
Source wave length/pulse width	200 nm/~300 fs, 266 nm/~170 fs	
Energy at source	200 nm/60 μJ, 266 nm/300 μJ	
Focusing lens	200 nm: Fluorite and fused silica combination objective lens	
	266 nm: Fused silica aspherical objective lens	
Spot size	200 nm: 20 μm on sample surface	
	266 nm: 50 μm on sample surface	
Fluence at laser spot	200 nm/~6 J cm^{-2}, 266 nm/~12 J cm^{-2}	
Repetition rate	200 nm/25–1 Hz, 266 nm/10–1 Hz	
Rotation raster radius	200 nm/7 μm, (266 nm/Line)	
Rotation/line raster velocity	7 μm s^{-1}	
He gas flow	1.15 L min^{-1}	
[MC-ICPMS]		
Equipment	Thermo Scientific NEPTUNE	
RF-power	1400 W	
Guard electrode	On	
Sampling cone	JET-sample cone (Ni)	
Skimmer cone	X-skimmer cone (Ni)	
Plasma gas (Ar)	1.0 L min^{-1}	
Laser carrier gas (Ar)	~1.3 L min^{-1}	
Interface vacuum with E2M80	1.7 mbar with He ablation carrier gas	
Baseline measurement	30 s × 2 on peak baseline before acquisition	
Acquisition	~0.5 s × 30 scans after 8 s idle time	
Faraday detector setting		
^{202}Hg	FC L3	(10^{12} Ω amplifier)
^{203}Tl	FC L2	(10^{11} Ω amplifier)
^{204}Pb (^{204}Hg)	FC L1	(10^{12} Ω amplifier)
^{205}Tl	FC Axial	(10^{11} Ω amplifier)
^{206}Pb	FC H1	(10^{13} Ω amplifier)
^{207}Pb	FC H2	(10^{13} Ω amplifier)
^{208}Pb	FC H3	(10^{13} Ω amplifier)
Zoom optics 1: Dispersion quad lens	0 V	
Zoom optics 2: Focus quad lens	7 V	
Data correction	off-line with Excel spreadsheet	

[a] FC: Faraday corrector; isobaric atomic and molecular ions are shown in parentheses

Table 2 Configurations of the Faraday amplifier combinations used for gain calibration[a]

Amplifier	Amp 1	Amp 2	Amp 3	Amp 4
Resistor	10^{12} Ω	10^{13} Ω	10^{13} Ω	10^{13} Ω
Isotope				
Cycle 1	^{143}Nd	^{144}Nd	^{146}Nd	
Cycle 2		^{143}Nd	^{144}Nd	^{146}Nd
Cycle 3	^{146}Nd		^{143}Nd	^{144}Nd
Cycle 4	^{144}Nd	^{146}Nd		^{143}Nd
Result	^{143}Nd/^{144}Nd		2 SE	
Initial measurement by 10^{11} Ω amplifiers				
	0.512211	±	0.000070	
Measurements by a 10^{12} Ω and three 10^{13} Ω amplifiers				
Cycle 1	0.504776	±	0.000080	
Cycle 2	0.522075	±	0.000032	
Cycle 3	0.510701	±	0.000100	
Cycle 4	0.511278	±	0.000127	
After calibration measurement by 10^{13} Ω amplifiers				
	0.512210	±	0.000033	
Amplifier	Amp 1	Amp 2	Amp 3	Amp 4
AGF (raw value)	0.996125	0.989874	1.006286	1.001044
AGF (Amp 1 relative)	0.099479	0.009885	0.010049	0.009967

[a] AGF: amplifier gain factor, 2 SE: 2 standard errors

Table 3 Representative analytical results for Pb isotope ratios in BHVO-2G and BCR-2G basalt glasses[a]

Sample	$^{208}Pb/^{206}Pb$	2 SD	$^{207}Pb/^{206}Pb$	2 SD	Reference
BHVO-2G					
10^{13} Ω amplifier	2.0470	± 0.0039 (1.9‰)	0.8325	± 0.0039 (0.6‰)	This work
MIC	2.0530	± 0.0180	0.8340	± 0.0080	Chang *et al.* (2014)[10]
10^{12} Ω amplifier	2.0481	± 0.0152	0.8339	± 0.0300	Kimura *et al.* (2015)[16]
LA-MFC-ICPMS	2.0557	± 0.0056 (2.7‰)	0.8336	± 0.0025 (3.0‰)	Zhang et al. (2014)[13]
Reference (2 SE)	2.0480	± 0.0030	0.8320	± 0.0010	Weis *et al.* (2006)[6]
BCR-2G					
10^{13} Ω amplifier	2.0632	± 0.0015 (1.2 ‰)	0.8324	± 0.0003 (0.7‰)	This work
10^{12} Ω amplifier	2.0607	± 0.0040	0.8324	± 0.0047	Kimura *et al.* (2015)[16]
Reference (2 SE)	2.0631	± 0.0014	0.8328	± 0.0005	Elburg *et al.* (2006)[25]

[a] Errors are given by 2 standard deviations (2 SD) for our work, whereas 2 standard errors (2 SE) are used for the reference data that were analysed by high-precision MC-ICPMS bulk analyses.

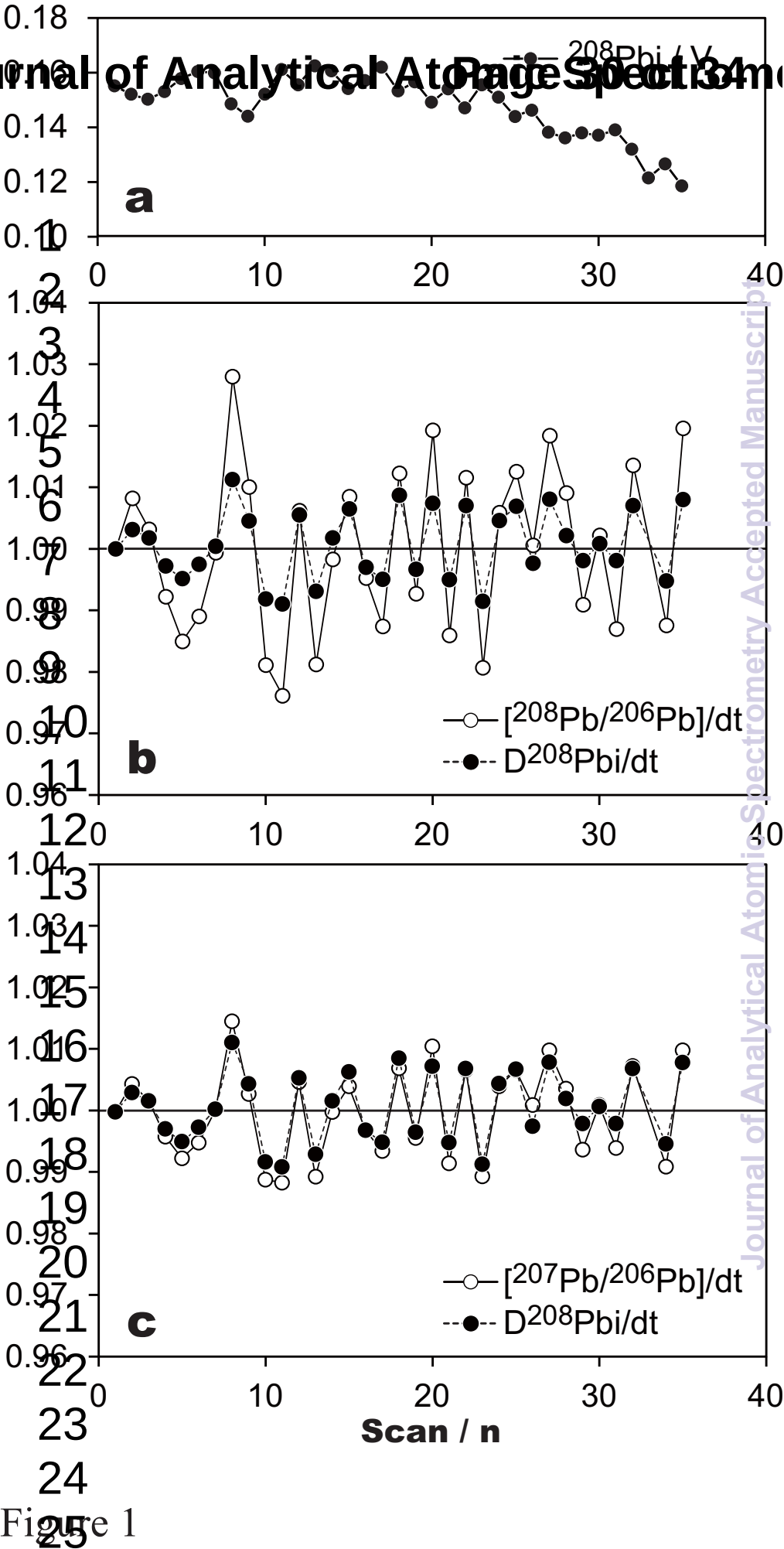

Figure 1

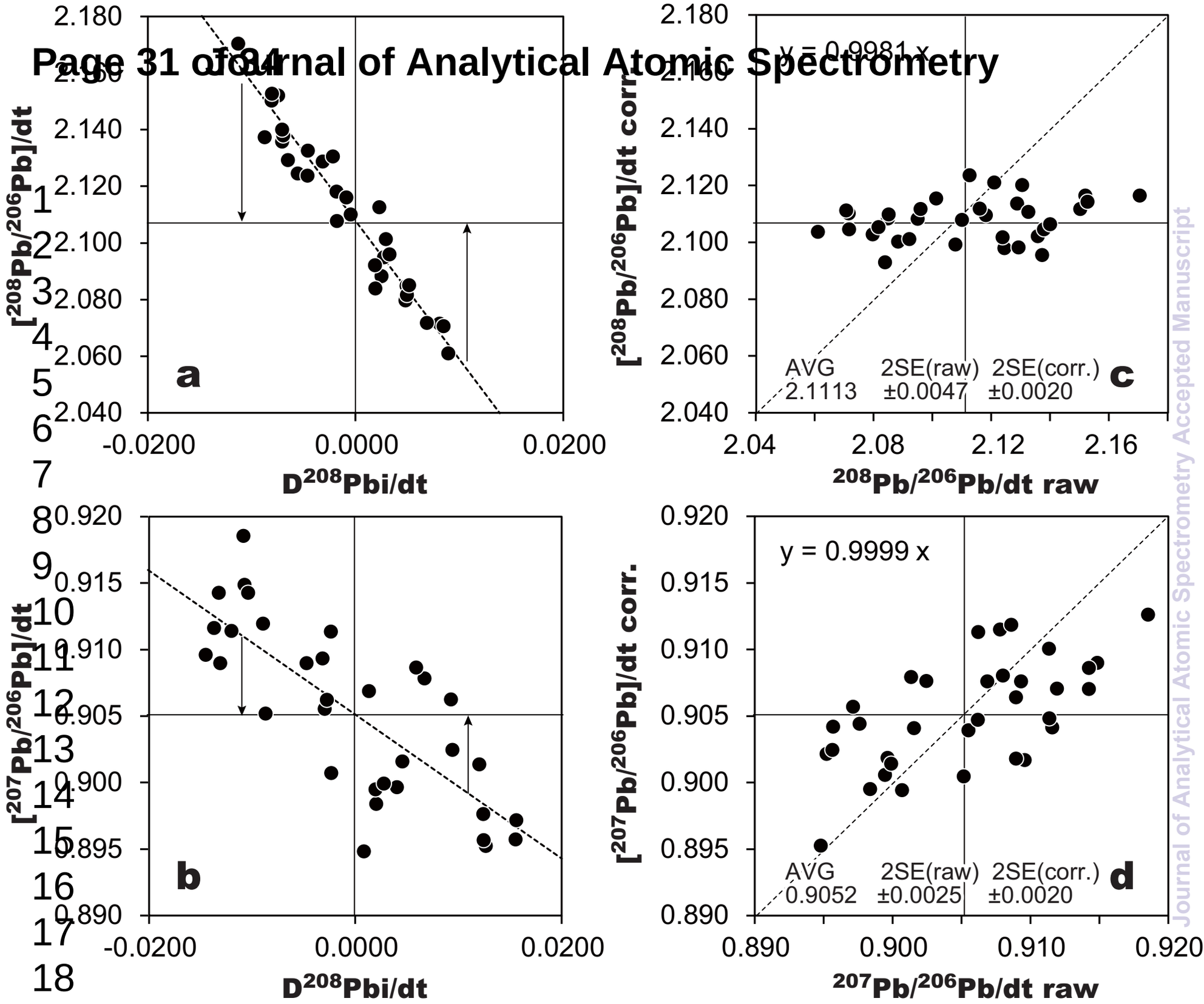

Figure 2

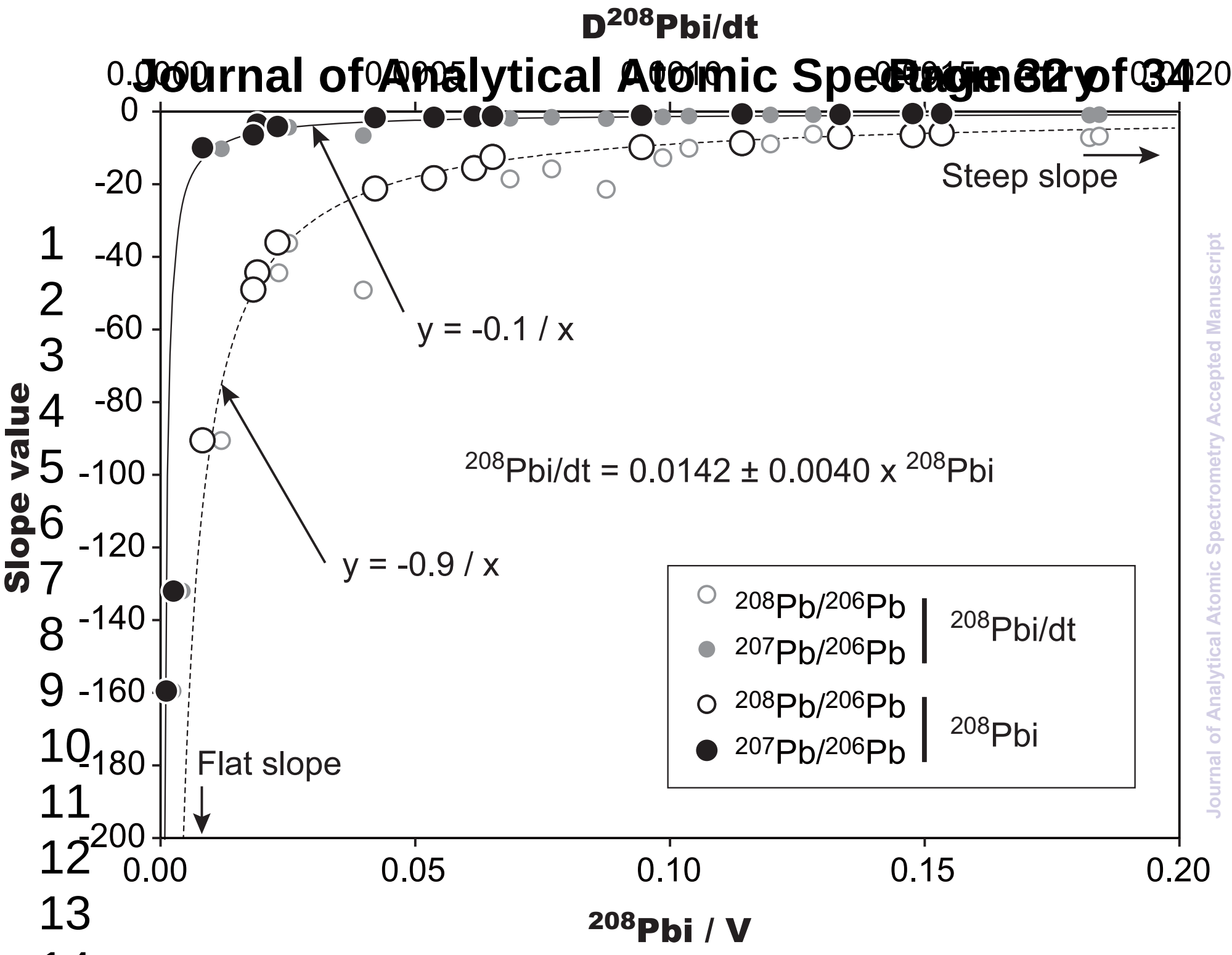

Figure 3

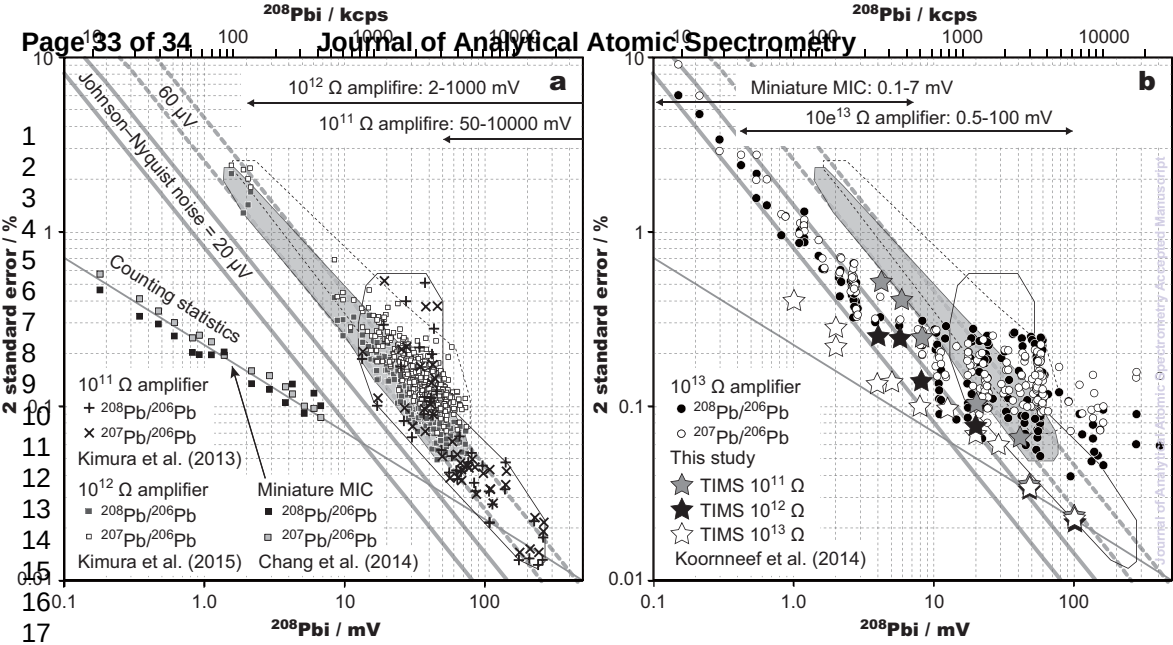
208Pbi / kcps
2 standard error / %
208Pbi / mV
a
10^12 Ω amplifire: 2-1000 mV
10^11 Ω amplifire: 50-10000 mV
Johnson–Nyquist noise = 20 µV
60 µV
Counting statistics
10^11 Ω amplifier
+ 208Pb/206Pb
× 207Pb/206Pb
Kimura et al. (2013)
10^12 Ω amplifier
208Pb/206Pb
207Pb/206Pb
Kimura et al. (2015)
Miniature MIC
208Pb/206Pb
207Pb/206Pb
Chang et al. (2014)
b
Miniature MIC: 0.1-7 mV
10e13 Ω amplifier: 0.5-100 mV
10^13 Ω amplifier
208Pb/206Pb
207Pb/206Pb
This study
TIMS 10^11 Ω
TIMS 10^12 Ω
TIMS 10^13 Ω
Koornneef et al. (2014)

Figure 4

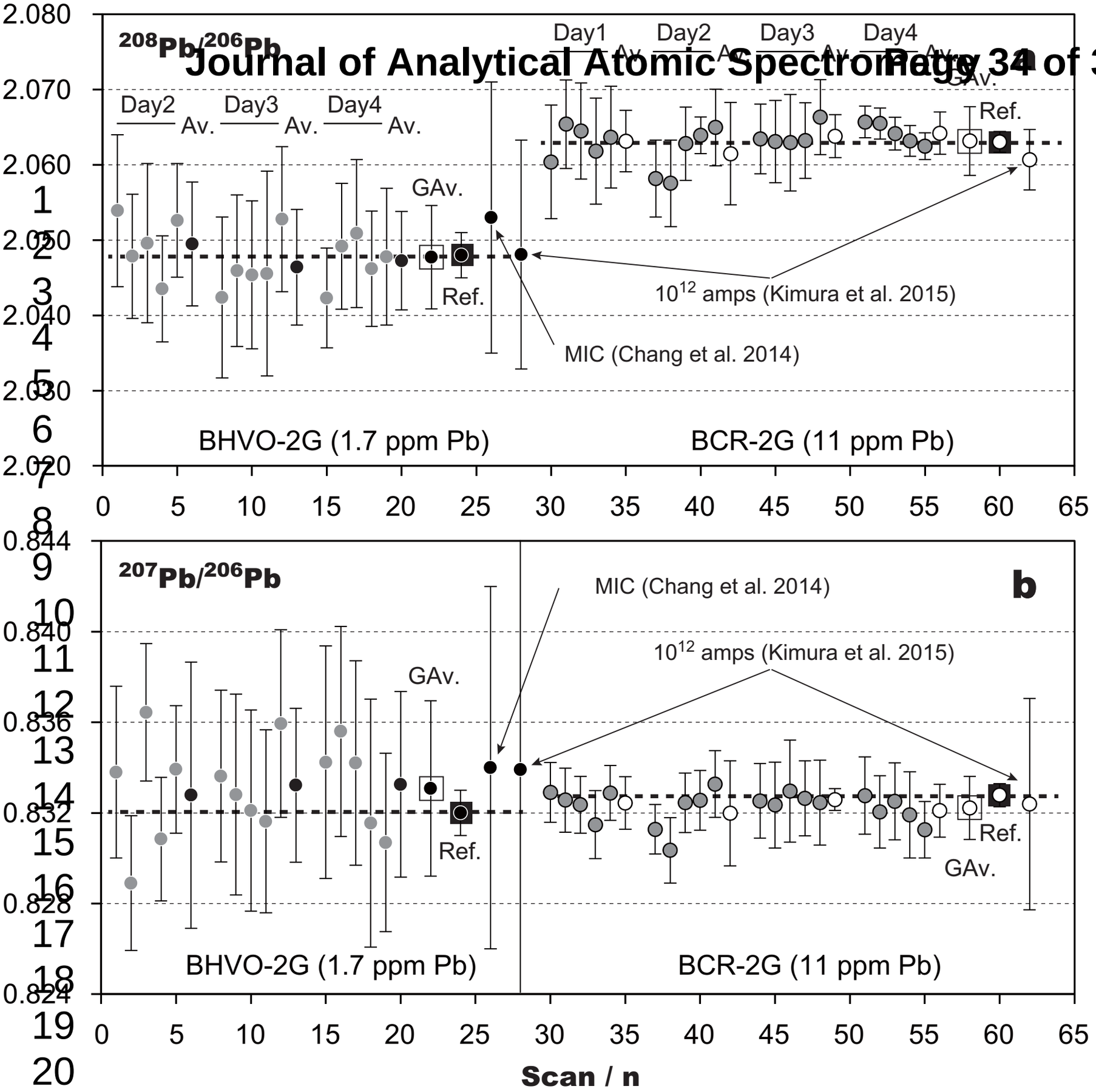

Figure 5